

www.acsami.org Research Article

# Producing Tunable Broadband Near-Infrared Emission through Co-Substitution in $(Ga_{1-x}Mg_x)(Ga_{1-x}Ge_x)O_3$ :Cr<sup>3+</sup>

Jiyou Zhong,\* Liwei Zeng, Weiren Zhao, and Jakoah Brgoch\*



Cite This: ACS Appl. Mater. Interfaces 2022, 14, 51157-51164



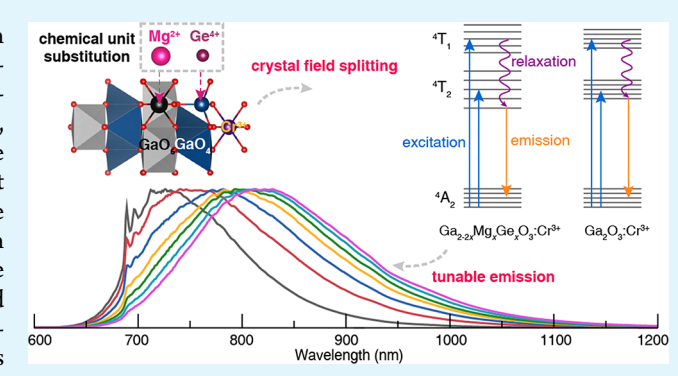
ACCESS I

Metrics & More

Article Recommendations

s Supporting Information

ABSTRACT: Broadband near-infrared (NIR) phosphors are in high demand for creating "smart" NIR phosphor-converted lightemitting diode (pc-LED) sources. In this work, a series of Cr3+substituted NIR-emitting materials with highly efficient, broad, tunable emission spectra are achieved by modifying the simple oxide  $Ga_2O_3$  using  $[Mg^{2+}-Ge^{4+}]$  and  $[Ga^{3+}-Ga^{3+}]$  co-unit substitution. The results show that the emission peak can be shifted from 726 to 830 nm while maintaining a constant excitation peak in the blue light region, enabling extensive application. The optical properties stem from changes in the Cr3+ crystal field environment upon substitution. Intriguingly, the temperaturedependent photoluminescence emission peak position shows virtually no change in the [Mg<sup>2+</sup>-Ge<sup>4+</sup>] co-substituted materials.



This abnormal phenomenon is found to be a comprehensive embodiment of a weakening crystal field environment (red-shift) as the temperature increases and reduced local structure distortion (blue-shift) with increasing temperature. The high quantum yield, NIR emission, and net-zero emission shift as a function of temperature make this phosphor class optimal for device incorporation. As a result, their performance was studied by coating the phosphor on a 450 nm emitting LED chip. The fabricated device demonstrates an excellent NIR output power and NIR photoelectric conversion efficiency. This study provides a series of efficient, tunable, broadband NIR materials for spectroscopy applications and contributes to the basic foundation of Cr<sup>3+</sup>-activated NIR phosphors.

KEYWORDS: co-substitution, photoluminescence, crystal field splitting, near-infrared, simple oxide

#### 1. INTRODUCTION

Near-infrared (NIR) spectroscopy has gained significant attention recently due to its widespread application in night vision, nondestructive food quality analysis, and nonradiative bioimaging. 1-4 The NIR region spanning ~700 to 1100 nm is particularly interesting because it covers the characteristic absorption signals of the C-H, O-H, and N-H normal vibrational modes, enabling many of these technologies.<sup>5,6</sup> As a result, maximum spectral coverage in this region requires ultrabroadband NIR light sources centered near  $\lambda_{\rm em,max} \approx 830$ nm.<sup>7,8</sup> The most promising method available today for generating long-wavelength light is by using NIR phosphorconverted light-emitting diodes (pc-LEDs). These devices are energy-efficient, have a compact size and high radiant flux, and have a tunable broadband emission in the correct device design. 11-13 New pc-LED NIR light sources would enable the production of portable smart devices for quick biosensing and daily use. 14,15 However, the output performance of the NIR pc-LED devices depends on the phosphor coating; thus, developing ultrabroadband and long-wavelength NIR phosphors is vital to advance this technology. 16-18

Trivalent chromium-substituted phosphors are considered the best NIR emitter for LED applications available today. They show excellent blue light ( $\lambda_{\rm ex} \approx 450$  nm) absorption, a high photoluminescence quantum yield (PLQY), and a tunable emission maximum depending on the crystal field environment. 19,20 Until recently, the development of red and NIR phosphors has traditionally focused on rare earth (Ce3+ and Eu<sup>2+</sup>) ions with strong-crystal field splitting, which greatly limited the plausible crystal chemistries. 21-24 Cr3+-activated phosphors are different. These materials require a weak octahedral crystal field to generate a long-wavelength NIR emission.<sup>25</sup> However, as the crystal field weakens, the excitation peak will be red-shifted, resulting in a mismatch with the blue LED chip. 26,27 The emission efficiency will also inevitably decrease with a weaker crystal field due to the enhanced nonradiative relaxation according to the theory of multiphonon radiative and nonradiative transitions caused by the narrowed energy gap between the ground state and the

Received: October 4, 2022 Accepted: October 26, 2022 Published: November 7, 2022





excited state.<sup>28</sup> Therefore, finding ways to achieve an appropriate crystal field environment, maintain efficient bluelight excitation, and simultaneously red-shift the emission spectrum remains a significant challenge.

Over the past several years, researchers have developed multiple workarounds to overcome the lack of optimal Cr<sup>3+</sup> coordination environments, including the "multiple-site strategy", Cr3+-Yb3+ energy transfer, and crystal field engineering, all of which have been applied to increase the coverage of long-wavelength NIR emission. <sup>29-34</sup> For example, La<sub>3</sub>Ga<sub>5</sub>GeO<sub>14</sub>:Cr<sup>3+</sup> and La<sub>2</sub>MgZrO<sub>6</sub>:Cr<sup>3+</sup> have full width at half maximum (FWHM) values of 330 and 210 nm, respectively, due to their multiple substitution sites. 35,36  $Ca_2LuZr_2Al_3O_{12}:Cr^{3+},Yb^{3+}, La_2MgHfO_6:Cr^{3+},Yb^{3+},$ LiIn<sub>2</sub>SbO<sub>6</sub>:Cr<sup>3+</sup>,Yb<sup>3+</sup>, and LiScP<sub>2</sub>O<sub>7</sub>:Cr<sup>3+</sup>,Yb<sup>3+</sup> each have a FWHM of over 210 nm benefiting from efficient Cr<sup>3+</sup>-Yb<sup>3+</sup> energy transfer.<sup>37–40</sup> Crystal field engineering was applied by forming solid solutions, like in Mg<sub>2-2x</sub>Li<sub>x</sub>Sc<sub>x</sub>GeO<sub>4</sub>:Cr<sup>3+</sup>, to shift the emission peak from 940 to 1110 nm and widen the corresponding FWHM from 236 to 300 nm. 41 Although most of these strategies are effective, the basic way to regulate the luminescence properties of Cr3+-activated material still depends on controlling the strength of the crystal field.

Recently, the simple oxide  $\beta$ -Ga<sub>2</sub>O<sub>3</sub> with a wide band gap  $(E_{\rm g}$  = 4.7-4.9 eV), appropriate structural rigidity, and reasonable crystal field environment proved to be a promising host for  $Cr^{3+}$ .  $^{42-44}$  The PLQY of  $Ga_2O_3$ : $Cr^{3+}$  was found to be 92%, although the emission peak was only located in the farred region ( $\lambda_{\text{em,max}} = 726 \text{ nm}$ ), limiting its versatility.<sup>45</sup> The emission peak center could be moved to 830 nm by weakening the crystal field splitting through the substitution of (ionically) larger elements, like Sc3+ or In3+. Solid solutions following  $Ga_{2-x}(Sc_1In)_xO_3:Cr^{3+}$  each demonstrated the ability to redshift the emission spectrum while maintaining the high PLQY  $(\geq 88\%)$ . However, even with the complete substitution of octahedral Ga<sup>3+</sup> by Sc<sup>3+</sup> or In<sup>3+</sup>, the peak wavelength cannot exceed 830 nm. <sup>46,47</sup> The full width at half maximum (FWHM) of the emission spectra is also relatively narrow (<160 nm). Moreover, In<sup>3+</sup> substitution dramatically narrows the band gap of the host material and red-shifts the excitation peaks, triggering a low PLQY and poor thermal stability. 46 Therefore, practical applications of this phosphor system require a different approach to red-shift the emission peak, maintain the excitation peak position, expand the FWHM, and maintain the high efficiency and high-temperature photoluminescence.

In this work, a new method based on chemical unit cosubstitution was developed to regulate the crystal field environment while maintaining the rest of the optical properties in the Ga<sub>2</sub>O<sub>3</sub>:Cr<sup>3+</sup> system. The approach reduces the variations of the crystal field environment by using the [Mg<sup>2+</sup>-Ge<sup>4+</sup>] ( $r_{6\text{-coor.}}$ (Mg<sup>2+</sup>) +  $r_{4\text{-coor.}}$ (Ge<sup>4+</sup>) = 1.11 Å) unit with similar size to substitute the [Ga<sup>3+</sup>-Ga<sup>3+</sup>] ( $r_{6\text{-coor.}}$ (Ga<sup>3+</sup>) +  $r_{4\text{-coor.}}$ (Ga<sup>3+</sup>) = 1.09 Å) unit in Ga<sub>2</sub>O<sub>3</sub>:Cr<sup>3+</sup>. Although the substitution ratio only reaches 20%, an optimal red-shift and FWHM are achieved. More importantly, the efficiency and thermal stability can be retained. A comprehensive investigation of the local structure and the crystal field environment around Cr<sup>3+</sup> provides insight into the mechanism(s) governing the change in optical properties. The product of this work includes a series of efficient long-wavelength ultrabroadband NIR materials. It also revises the fundamental understanding of Cr3+ luminescence, including a new approach for tuning the

optical properties using co-substitution, which is important for future NIR materials design.

#### 2. EXPERIMENTAL SECTION

- 2.1. Synthesis. The polycrystalline powder samples were all synthesized using a one-step high-temperature solid-state reaction method. First, the raw materials including Ga<sub>2</sub>O<sub>3</sub> (Aladdin, 99.99%), MgO (Aladdin, 99.99%), GeO<sub>2</sub> (Aladdin, 99.99%), In<sub>2</sub>O<sub>3</sub> (Aladdin, 99.99%), and Cr<sub>2</sub>O<sub>3</sub> (Aladdin, 99.99%) were weighed out according to the stoichiometric ratio. Then, the powders were mixed and ground for half an hour with an agate mortar and pestle. The mixtures were transferred to corundum crucibles and put into a muffle furnace. The furnace first increased the temperature to 1300 °C with a heating rate of 5 °C/min, which was then held for 6 h under air. The furnace was naturally cooled down to room temperature, and the products were removed and ground into fine powders with an agate mortar and pestle for subsequent measurement. The preparation of LiIn-Si<sub>2</sub>O<sub>7</sub>:Cr<sup>3+</sup> phosphor is based on the relevant literature.<sup>4</sup>
- 2.2. Characterization. Sample phase purity was first checked by powder X-ray diffraction collected on a laboratory X-ray diffractometer (X'pert, PRO, PANalytical, Netherlands,  $\lambda = 1.54$  Å). Rietveld refinement was performed by using the software of GSAS.<sup>50</sup> The crystal structure was analyzed and visualized by VESTA. Electron paramagnetic resonance (EPR) spectroscopy was performed on an EPR spectrometer (JES-FA300, Japan) at 77 K. The diffuse reflectance (DR) spectra were collected on a UV-vis-NIR spectrophotometer (Shimadzu, Japan). The photoluminescence excitation and emission spectra at different temperatures as well as the decay curves were obtained on an FLS-980 fluorescence spectrophotometer (Edinburgh Instruments), while the photoluminescence quantum yields and absorption of all these samples were measured by using an absolute photoluminescence quantum yield measurement system (Quantaurus-QY Plus C13534-12, Hamamatsu Photonics). The prototype NIR pc-LED devices were fabricated by coating a mixture of the phosphors and resin with a 1:1 ratio (by weight) on 450 nm blue LED chips (Epistar). The input and output parameters and the electroluminescence spectra of the fabricated NIR pc-LEDs were measured using a HAAS2000 photoelectric measuring system (EVERFINE, China).
- **2.3. Computation.** The structural models  $(1 \times 2 \times 2 \text{ supercell})$  of  $Ga_{2-2x}Mg_xGe_xO_3$  (x = 0, 0.0625, 0.125, 0.1875, and 0.25) were constructed and optimized using the Vienna ab initio Simulation Package (VASP),<sup>51</sup> which is a plane-wave pseudopotential total energy package based on density functional theory (DFT).<sup>52</sup> The atomic positions and lattice parameters were relaxed with an electronic convergence criterion of  $1\times10^{-5}$  eV and an atomic convergence criterion of 0.01 eV Å<sup>-1</sup>. The cutoff energy of 500 eV was used for the basis set of the plane waves, and a  $4 \times 2 \times 4$   $\Gamma$ centered Monkhorst-Pack k-point grid was used to sample the first Brillouin zone. The Perdew-Burke-Ernzerhof (PBE) exchangecorrelation functional was employed for structure optimization and stress tensor calculation to estimate the Debye temperature. 53-

#### 3. RESULTS AND DISCUSSION

3.1. Crystal Structure, Site Occupation, and Morphology. Figure 1a presents the powder X-ray diffractograms of  $Ga_{1.97-2x}Mg_xGe_xCr_{0.03}O_3$  (x = 0, 0.02, 0.04, 0.08, 0.12, 0.16, and 0.2). Each diffractogram can be indexed to  $\beta$ -Ga<sub>2</sub>O<sub>3</sub> (ICSD no. 15647), indicating that the phase pure samples have been successfully synthesized. Further increasing the substitution ratio will cause the presence of the MgGa<sub>2</sub>O<sub>4</sub> spinel phase, indicating that the solubility limit is ~20 mol % [Ga<sup>3+</sup>-Ga<sup>3+</sup>] units being substituted by [Mg<sup>2+</sup>-Ge<sup>4+</sup>] units in  $\beta$ -Ga<sub>2</sub>O<sub>3</sub>. To confirm the crystal structure and phase purity, the Rietveld refinement of the  $Ga_{1.97-2x}Mg_xGe_xCr_{0.03}O_3$  (x = 0 and 0.2) powder X-ray diffractograms was performed as shown in Figure 1b and Figure S1. The refined crystal structure, atomic

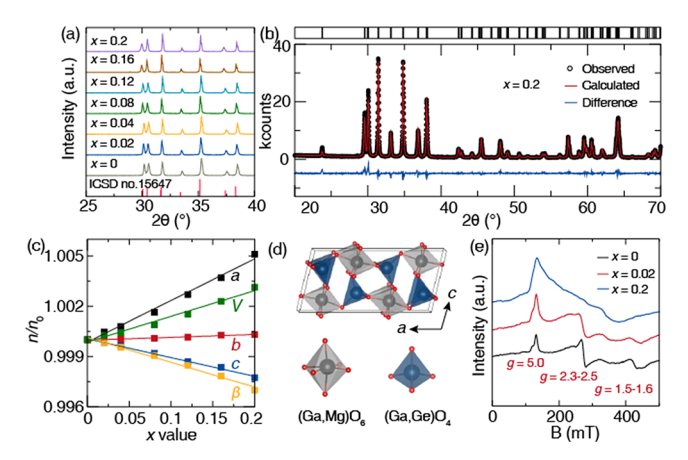


Figure 1. (a) Powder X-ray diffractograms of  $Ga_{1.97-2x}Mg_xGe_xCr_{0.03}O_3$  (x = 0, 0.02, 0.04, 0.08, 0.12, 0.16, and 0.2) samples comparing with the standard card of  $\beta$ -Ga<sub>2</sub>O<sub>3</sub> (ICSD no. 15647). (b) Rietveld refinement of the powder X-ray diffractogram for the Ga<sub>1.57</sub>Mg<sub>0.2</sub>Ge<sub>0.2</sub>Cr<sub>0.03</sub>O<sub>3</sub> sample. (c) Refined (normalized) unit cell parameters as a function of x value. (d) Refined crystal structure of  $Ga_{1.57}Mg_{0.2}Ge_{0.2}Cr_{0.03}O_3$  and coordination environment of cations. (e) EPR spectrum of  $Ga_{1.97-2x}Mg_xGe_xCr_{0.03}O_3$  (x = 0, 0.02, and 0.2) samples.

positions, and local coordination of the octahedral site are provided in Tables S1-S3, respectively. The acceptable refinement statistics demonstrate the high purity of the samples and support the structural model. Varying the xvalue from 0 to 0.2 in Ga<sub>1.97-2x</sub>Mg<sub>x</sub>Ge<sub>x</sub>Cr<sub>0.03</sub>O<sub>3</sub> causes the cell parameters to vary linearly (Figure 1c), supporting the successful incorporation of [Mg<sup>2+</sup>-Ge<sup>4+</sup>]. Notably, the lattice parameter a increases, and c decreases, while b is nearly unchanged as x increases. These results are different from the linear increase in the lattice parameters (a, b, and c) in  $Ga_{2-x}In_xO_3$ :  $Cr^{3+}$  or  $Ga_{2-x}Sc_xO_3$ :  $Cr^{3+}$ , implying a different behavior for co-substitution. Nevertheless, the parameters change by only 0.5% due to the relatively similar size between the  $[Mg^{2+}-Ge^{4+}]$  unit (1.11 Å) and the  $[Ga^{3+}-Ga^{3+}]$  unit (1.09 Å). $^{48}$ 

Visualizing the refined crystal structure (Figure 1d) indicates that  $Mg^{2+}$  and  $Ge^{4+}$  substitute on the  $Ga^{3+}$  octahedral and tetrahedral sites, respectively. This is verified by comparing the experimentally refined goodness-of-fit parameters for all possible  $Mg^{2+}$  and  $Ge^{4+}$  substitution patterns (Table S4).  $Mg^{2+}$  ( $r_{6\text{-coor.}} = 0.72 \text{ Å}$ ) is larger than  $Ga^{3+}$  ( $r_{6\text{-coor.}} = 0.62 \text{ Å}$ ) on an octahedral site, whereas  $Ge^{4+}$  ( $r_{4-coor.} = 0.39$  Å) is smaller than  $Ga^{3+}$  ( $r_{4-coor.} = 0.47$  Å) on a tetrahedral site, <sup>48</sup> leading to the observed changes in lattice parameters. The Cr3+ site occupancy cannot be determined from the refinement with such a low substitution concentration. Instead, the substitution site preference and the local structure of Cr3+ were determined by analyzing  $Ga_{1.97-2x}Mg_xGe_xCr_{0.03}O_3$  (x = 0, 0.02, and 0.2) using electron paramagnetic resonance (EPR). As shown in Figure 1e, when x = 0, the EPR signal shows g-factors of 5.0, 2.3-2.5, and 1.5-1.6, which belong to Cr3+ in isolated octahedral sites at different magnetic induction.<sup>47</sup> These resonances are consistent with previous reports and support that Cr<sup>3+</sup> does not occupy the tetrahedral site or form Cr<sup>3+</sup>-Cr<sup>3+</sup> ion pars.<sup>47</sup> Increasing [Mg<sup>2+</sup>-Ge<sup>4+</sup>] substitution shows a consistent number of peaks, suggesting that the initial cosubstitution does not change the  $Cr^{3+}$  site preference. However, the peak shapes change. This stems from a moderate local structural distortion with substitution or from a second

coordination sphere as Cr3+ shifts from a single type of Ga-Cr-Ga environment to a mixture of Ga-Cr-Ga, Ga-Cr-Mg, and Mg-Cr-Mg. The EPR signal captures this disorder as a broad signal.

The morphology of Ga<sub>1.57</sub>Mg<sub>0.2</sub>Ge<sub>0.2</sub>Cr<sub>0.03</sub>O<sub>3</sub> was examined by a SEM image, as shown in Figure S2a. The particles tend to present irregular shapes with an average size of  $\sim 3 \mu m$ . EDS mapping of the elemental distribution on randomly selected crystallites (Figure S2b) shows that all the elements loaded in this material can be detected and are uniformly distributed, further directly proving the success of introducing the Mg<sup>2+</sup>-Ge<sup>4+</sup>] unit and Cr<sup>3+</sup> into the lattice of Ga<sub>2</sub>O<sub>3</sub>.

3.2. Reflectivity and Tunable Photoluminescence. The diffuse reflection (DR) spectra of  $Ga_{2-2x}Mg_xGe_xO_3$  (x = 0and 0.2) hosts and  $Ga_{1.97-2x}Mg_xGe_xCr_{0.03}O_3$  (x = 0, 0.12, and 0.2) phosphors are presented in Figure 2a. A slight red-shift of

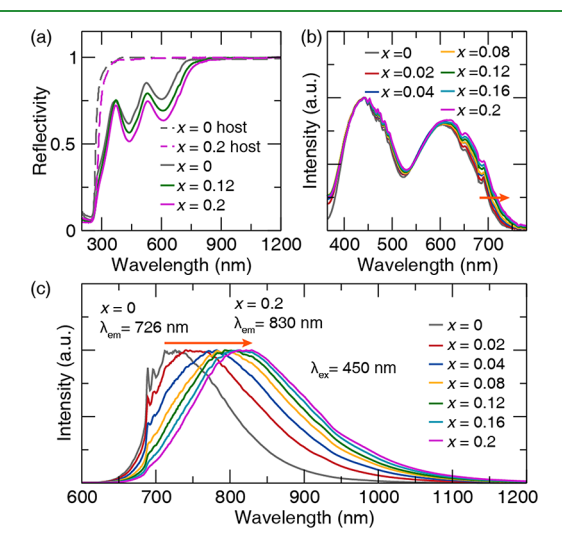


Figure 2. (a) Diffuse reflection spectra of  $Ga_{2-2x}Mg_xGe_xO_3$  (x = 0and 0.2) hosts and  $Ga_{1.97-2x}Mg_xGe_xCr_{0.03}O_3$  (x = 0, 0.12, and 0.2) phosphors. Normalized (b) excitation spectra and (c) emission spectra of  $Ga_{1.97-2x}Mg_xGe_xCr_{0.03}O_3$  (x = 0-0.2) phosphors.

the DR spectra can be observed after [Mg<sup>2+</sup>-Ge<sup>4+</sup>] is incorporated into Ga2O3, implying the optical band gap narrowing from 4.73 to 4.63 eV, as measured from the Kubelka-Munk transformed absorption spectrum (Figure S3).<sup>56</sup> This decrease (0.1 eV) of the band gap is almost neglectable compared to the changes caused by  ${\rm In^{3+}}$  or  ${\rm Sc^{3+}}$  substituted in  ${\rm Ga_2O_3.}^{46,47}$  Measuring the DR spectra upon varying x in  $Ga_{1.97-2x}Mg_xGe_xCr_{0.03}O_3$  (x = 0, 0.12, and 0.2) indicated that the two absorption bands, which can be assigned to the  ${}^4A_2 \rightarrow {}^4T_1$  ( ${}^4F$ ) and  ${}^4A_2 \rightarrow {}^4T_2$  ( ${}^4F$ ) transitions of  $Cr^{3+}$ , remain nearly constant.<sup>57</sup> Interestingly, the absorptivity does increase with increasing x. This surprising result must stem from the introduction of odd-parity to break the parityforbidden nature of Cr3+ 3d-3d electronic transitions, which can only arise from a distortion in the local coordination environment.5

The normalized photoluminescence excitation spectra of  $Ga_{1.97-2x}Mg_xGe_xCr_{0.03}O_3$  (x = 0, 0.02, 0.04, 0.08, 0.12, 0.16, and 0.2) are illustrated in Figure 2b. The excitation peak in the blue region does not change regardless of the x value, while the excitation band in the red region shows a slight shift to lower energy due to peak broadening. These results are consistent with the DR spectra, suggesting that a minor influence on the

strength of the crystal field is generated by the [Mg<sup>2+</sup>-Ge<sup>4+</sup>] unit co-substitution. <sup>59</sup> Upon 450 nm excitation, the normalized photoluminescence emission spectra (Figure 2c) indicate a tunable emission as a function of [Mg<sup>2+</sup>-Ge<sup>4+</sup>]. As shown in Figure S4, the emission peak can be significantly red-shifted from 726 to 830 nm, while the FWHM can be extended from 122 to 186 nm (2201.0 to 2714.4 cm<sup>-1</sup>) as the *x* value increases from 0 to 0.2. Although the increased FWHM is beneficial to its spectral coverage in the NIR region, it is also a reflection of enhanced electron—lattice coupling, which may increase the probability of radiative transitions.

Such a significant red-shift and broadening of the emission spectrum are well beyond expectation. The crystal field was not expected to weaken with [Mg<sup>2+</sup>-Ge<sup>4+</sup>] based on the DR as much as is observed. It is therefore vital to identify the mechanism leading to this response. Generally, there are two considerations for red-shifting the emission spectrum of Cr<sup>3+</sup>-activated materials. One involves the coupling of Cr<sup>3+</sup>-Cr<sup>3+</sup> ion pairs, <sup>60</sup> which will induce significant energy level splitting due to the strong exchange interactions between Cr<sup>3+</sup>-Cr<sup>3+</sup>, whereas the other is through the weakening of the crystal field environment. <sup>61-63</sup> The EPR spectrum does not support the presence of Cr<sup>3+</sup>-Cr<sup>3+</sup> ion pairs, and the nearly unchanged absorption (DR and excitation peaks) indicates an essentially constant crystal field environment. Thus, the red-shift caused by [Mg<sup>2+</sup>-Ge<sup>4+</sup>] co-substitution must follow a different mechanism.

As we known, the emission of rare earth ion Eu<sup>2+</sup> with 4f  $\leftrightarrow$ 5d transitions can also be affected by crystal field strength and symmetry, changing the centroid shift and energy levels' splitting, respectively. Similarly, the crystal field strength and symmetry can also influence the centroid shift and energy levels' splitting of  $Cr^{3+}$  with 3d  $\leftrightarrow$  3d transitions. Weakening the crystal field strength is well accepted as a regulation method for tuning the emission and excitation spectrum of Cr3+ toward a longer wavelength. Reducing the crystal field symmetry through a local structure distortion that will change the photoluminescence spectrum is unknown. Herein, we propose that a local structure distortion should be responsible for this red-shift of emission spectra (Figure 3a). In this mechanism, the degenerate energy levels will split, while the other energy levels will show an enlarged degree of splitting by incorporating  $[Mg^{2+}\text{-}Ge^{4+}]$  co-substitution (with a neglectable centroid shift). This will allow the excited electrons to relax to a lower energy level and produce the observed red-shifted emission spectrum while maintaining the excitation energy.

This hypothesis is supported by first eliminating the influence of crystal field effects. A smaller co-substitution, the  $[Mg^{2+}-Si^{4+}]$  unit (0.98 Å) for the  $[Ga^{3+}-Ga^{3+}]$  unit (1.09 Å), was therefore tested.<sup>48</sup> The synthesis of phosphors following  $Ga_{1.97-2x}Mg_xSi_xCr_{0.03}O_3$  showed a solubility limit of  $\leq 12$  mol % (Figure S5). The unit cell volume shows a linear decrease as the co-substituting ratio increases (Figure S6), which should generate a stronger crystal field environment and blue-shift the emission spectrum. The excitation spectra (Figure S7a) of  $Ga_{1.97-2x}Mg_xSi_xCr_{0.03}O_3$  (x = 0, 0.02, 0.04, 0.08, and 0.12) also show a nearly unchanged spectrum, although there is slight broadening. Under 450 nm excitation, the emission spectra (Figure S7b) of  $Ga_{1.97-2x}Mg_xSi_xCr_{0.03}O_3$  (x = 0, 0.02, 0.04,0.08, and 0.12) also exhibit a significant red-shift from 726 to 794 nm. Considering that the excitation and emission spectrum of [Mg<sup>2+</sup>-Si<sup>4+</sup>] co-substituted systems is nearly identical to that of the [Mg<sup>2+</sup>-Ge<sup>4+</sup>] co-substituted materials,

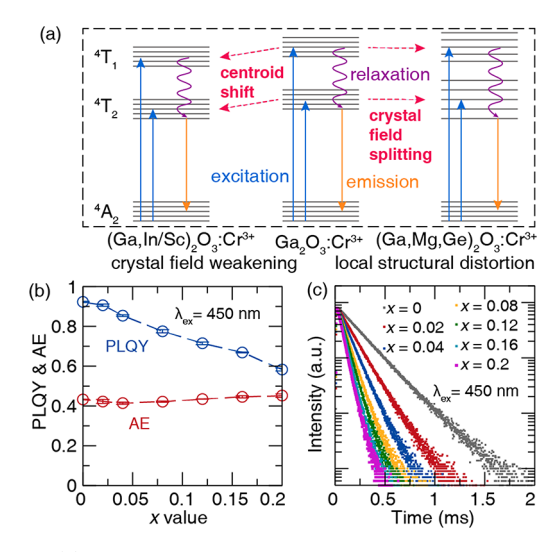


**Figure 3.** (a) Crystal field splitting model and centroid shift model for  $Cr^{3+}$  caused by local structural distortion and crystal field weakening, respectively. (b) Photoluminescence quantum yield and absorption efficiency and (c) decay curves of  $Ga_{1.97-2x}Mg_xGe_xCr_{0.03}O_3$  (x = 0-0.2) phosphors.

the dominant mechanism for red-shifting the emission spectrum must be similar.

To further test the two mechanisms in this material system, a series of  $[Mg^{2+}-Ge^{4+}-In^{3+}]$  co-substituted materials with the formula  $Ga_{1.97-2x-y}Mg_xGe_xIn_yCr_{0.03}O_3$  were proposed. Fixing x=0.16 and varying y=0 to 0.6 show an even more dramatic red-shift in the emission spectrum from 813 to 920 nm. This wavelength simultaneously guarantees the excitation peak with  $^4A_2 \rightarrow {}^4T_1$  transition located in the blue region of the electromagnetic spectrum (Figure S8). This result also demonstrates the ability of the  $Ga_2O_3$ : $Cr^{3+}$  system to break the current limit of long-wavelength NIR emission in the first biowindow.

The photoluminescence quantum yield (PLQY) and absorption efficiency (AE) of  $Ga_{1.97-2x}Mg_xGe_xCr_{0.03}O_3$  (x=0,0.02,0.04,0.08,0.12,0.16, and 0.2) were measured as shown in Figure 3b. The PLQY gradually decreases from 92.3 to 58.3%, while the absorption efficiency increases from 43.3 to 45.2% as x goes from 0 to 0.2. The decrease in PLQY can be mainly ascribed to the gradually enhanced lattice—electron coupling effect, which can be deduced from the dramatically increased FWHM of the emission spectra, increasing the energy loss in the pathway of the nonradiative relaxation process. The increase in AE is mainly due to the introduction of odd-parity to break the parity-forbidden nature of  $Cr^{3+}$  3d-3d electronic transitions. He henomena must arise from the lattice distortions around  $Cr^{3+}$  induced by  $[Mg^{2+}-Ge^{4+}]$  unit incorporation.

The gradually enhanced nonradiative relaxation process can be deduced from the decay behavior as depicted in Figure 3c. Fitting the decay curves with a single-exponential function (Figure S9), the lifetime drops from 221.2 to 55.9  $\mu$ s as the [Mg<sup>2+</sup>-Ge<sup>4+</sup>] co-substitution ratio increases. This behavior differs from Ga<sub>2-x</sub>In<sub>x</sub>O<sub>3</sub>:Cr<sup>3+</sup> or Ga<sub>2-x</sub>Sc<sub>x</sub>O<sub>3</sub>:Cr<sup>3+</sup>, which require a multi-exponential fit. He incorporation of [Mg<sup>2+</sup>-Ge<sup>4+</sup>] did not change the preference of Cr<sup>3+</sup>—it always occupies the octahedral Ga<sup>3+</sup> site due to their similar ionic size and valence state. He is a single relaxation process can be deduced in Figure 3c.

**3.3. Thermal Stability.** The thermal stability of phosphor is among the most important criteria for future application. This is particularly true for phosphors with a huge Stokes shift like  $Cr^{3+}$  that will generate additional heat when converting blue light into NIR light. The temperature dependence of the emission spectra for  $Ga_{1.97-2x}Mg_xGe_xCr_{0.03}O_3$  with x=0 and 0.2 is shown as a contour plot (Figure 4a,b, respectively).

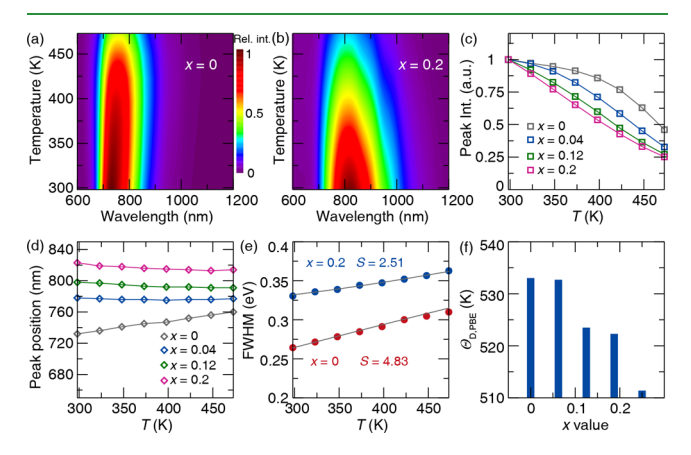


**Figure 4.** Contour plot of the emission spectra of  $Ga_{1.97-2x}Mg_xGe_xCr_{0.03}O_3$  with (a) x=0 and (b) x=0.2 as a function of temperature. Emission peak (c) intensity and (d) position of  $Ga_{1.97-2x}Mg_xGe_xCr_{0.03}O_3$  (x=0, 0.04, 0.12, and 0.2) as a function of temperature. (e) Fitting the relationship between FWHM and T for  $Ga_{1.97-2x}Mg_xGe_xCr_{0.03}O_3$  (x=0 and 0.2). (f) DFT-PBE-calculated Debye temperature for  $Ga_{2-2x}Mg_xGe_xO_3$  (x=0, 0.0625, 0.125, 0.1875, and 0.25).

The emission peak intensity (the integral intensity is shown in Figure S10) when x=0, 0.04, 0.12, and 0.2 is plotted as a function of temperature in Figure 4c. The emission peak intensity at 423 K ( $I_{423\text{K}}$ ), the approximate working temperature of an LED-based device, remains at 77% at room temperature when x=0. The increase in x causes the  $I_{423\text{K}}$  to gradually decrease from 58.5 to 47.3 to 42.8% for x=0.04, 0.12, and 0.2, respectively. The emission peak position as a function of temperature is shown in Figure 4d. When x=0, the emission peak presents a significant red-shift (726 to 760 nm)

with the increase in temperature, which should stem from a weaker crystal field environment due to temperature-dependent lattice expansion. However, for x = 0.04, 0.12, and 0.2, the peak positions remain unchanged or exhibit a slight blue-shift with an increase in temperature. This abnormal phenomenon is a comprehensive embodiment of a weakening crystal field environment (red-shift) as the temperature increases and reduced local structure distortion (blue-shift) with increasing temperature, which can be verified by the temperature-dependent unit-cell volume and distortion index (Figure S11), derived from refinements of temperature-dependent XRD data of  $Ga_{1.57}Mg_{0.2}Ge_{0.2}Cr_{0.03}O_3$  (Figure S12).

Minimizing the change in the emission peak is undoubtedly useful, while the rapid decrease in emission intensity is harmful to the application of this material. The thermal quenching of  $Cr^{3+}$ -activated material is closely related to the electron–phonon coupling (EPC) effect, which can be represented by the Huang–Rhys factor (S). The Huang–Rhys factor can be determined by fitting the relationship between the FWHM of the emission spectra and the temperature following eq 1, 28

$$FWHM (T) = \sqrt{8 \ln 2} \times h\nu \times \sqrt{\coth(h\nu/2kT)}$$
 (1)

where FWHM (eV) refers to the full width at half maximum of the emission spectrum at a given temperature, T (K). The hv and k represent the phonon energy and Boltzmann's constant, respectively. Fitting this equation (Figure 4e), the obtained Huang–Rhys factor values were 4.83 and 2.51 for x=0 and 0.2 samples, respectively, demonstrating a significant decrease in the electron–phonon coupling with the  $[Mg^{2+}-Ge^{4+}]$  unit incorporation. These results cannot support the observed change in temperature-dependent photoluminescence as a function of temperature, indicating the failure of Huang-Rhys factor in describing electron-phonon coupling effect in a material system with significant local structure distortion.

Moreover, the host crystal's structural rigidity and band gap are important for thermal quenching. Structural rigidity, represented by the material's Debye temperature  $(\Theta_D)$ , is closely related to the compound's vibration energy. A highly rigid structure is conducive to suppressing the nonradiative relaxation process. Figure 4f presents the theoretically calculated Debye temperature for

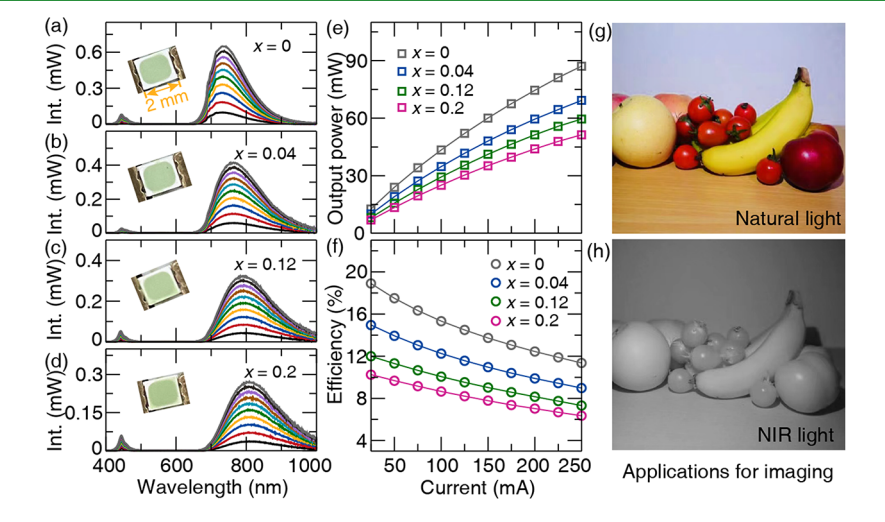


Figure 5. (a–d) Electroluminescence spectra of  $Ga_{1.97-2x}Mg_xGe_xCr_{0.03}O_3$  (x = 0, 0.04, 0.12, and 0.2) phosphors with the insets showing the corresponding NIR pc-LEDs. (e) NIR output power and (f) NIR photoelectric conversion efficiency of  $Ga_{1.97-2x}Mg_xGe_xCr_{0.03}O_3$  (x = 0, 0.04, 0.12, and 0.2) as a function of driving current. Photographs of fruit captured under (g) natural light and (h) NIR light of the fabricated NIR pc-LED.

 $Ga_{2-2x}Mg_xGe_xO_3$  (x = 0, 0.0625, 0.125, 0.1875, and 0.25). Although the Debye temperature decreases as x increases, the value remains high (above 510 K). Notably, the experimental band gap value for x = 0.2 is only 0.1 eV lower than that with x= 0, demonstrating that the band gap is not significantly narrowed with [Mg<sup>2+</sup>-Ge<sup>4+</sup>] unit incorporation and remains wide enough to resist thermal quenching through the pathway of thermal ionization.<sup>28</sup> Therefore, the dominant factor that should be responsible for the degradation of thermal stability after [Mg<sup>2+</sup>-Ge<sup>4+</sup>] unit co-substitution needs further explora-

3.4. NIR pc-LED Fabrication and Application. The device performance of  $Ga_{1.97-2x}Mg_xGe_xCr_{0.03}O_3$  (x = 0, 0.04, 0.12, and 0.2) was evaluated by coating the luminescent materials on 2 mm blue LED chips, which would make them viable NIR light sources in portable smart devices. The prototype NIR pc-LEDs and electroluminescence spectra are presented in Figure 5a-d, while the NIR output power and NIR photoelectric conversion efficiency are plotted in Figure 5e,f, respectively. The visual appearance of these phosphors is nearly identical, displaying a light green body color. The NIR output power increases as a function of driving current in the range of 25 to 250 mA and does not reach saturation. The NIR photoelectric conversion efficiency decreases as the driving current increases, mainly due to the lower efficiency of the LED chip. 66 Under 100 mA driving current, the NIR output power values are measured to be 43.4, 34.8, 29.4, and 25.1 mW, and the corresponding NIR photoelectric conversion efficiency values are determined to be 15.3, 12.3, 10.1, and 8.7%, for x = 0, 0.04, 0.12, and 0.2, respectively. The origin of the observed decrease in NIR output power and NIR photoelectric conversion efficiency stems from the gradually decreasing PLQY, although some of the drop is an experimental artifact due to the lack of spectral coverage in the measurement above 1000 nm. Nevertheless, the NIR output power and photoelectric conversion efficiency of all these devices are better than those fabricated by using the wellknown efficient LiInSi<sub>2</sub>O<sub>7</sub>:Cr<sup>3+</sup> phosphor (24.5 mW@8.7%, driven by 100 mA) under the same conditions as shown in Figure S13, demonstrating the excellent fabrication performance of this series of materials.

Finally, the practical application of a fabricated NIR pc-LED (x = 0.2) was demonstrated in imaging. The photographs of fruit captured under natural light and NIR light of the fabricated NIR pc-LED are shown in Figure 5g,h, respectively. As shown, the black-and-white images of fruit can be easily resolved under the exposure of NIR light generated by this prototype device. These results indicate that these materials may have a good potential for spectroscopy applications.

# 4. CONCLUSIONS

In summary, a series of  $Ga_{1.97-2x}Mg_xGe_xCr_{0.03}O_3$  (x = 0, 0.02,0.04, 0.08, 0.12, 0.16, and 0.2) phosphors with tunable broadband NIR emission were obtained by using chemical unit co-substitution. As x increases, the emission peak can be tuned up to 830 nm and the FWHM can be expanded, covering 186 nm (2714.4 cm<sup>-1</sup>). The crystal field splitting model was proposed to explain the red-shift of the emission spectrum, while additional signatures in the photoluminescence spectra indicate a concurrent local structural distortion. The photoluminescence quantum yield and thermal stability also show a decrease with increasing x, although the absolute values remain acceptable and can be improved. The nearly unchanged

emission peak position results from a weakened crystal field and reduced local structure distortion with increasing temperature. The degradation of thermal stability induced by cosubstitution cannot simply ascribed to the variation in electron-phonon coupling effect, a decrease in the host's structural rigidity or slightly narrowed band-gap. Finally, the fabricated NIR pc-LED exhibits excellent imaging performance, demonstrating these materials' great potential for NIR spectroscopy applications in portable smart devices.

#### ASSOCIATED CONTENT

### Supporting Information

The Supporting Information is available free of charge at https://pubs.acs.org/doi/10.1021/acsami.2c17902.

Rietveld refinement and refined results, optical band gap, emission peak position and FWHM, XRD patterns, lattice parameters, distortion index, excitation and emission spectra, decay curves, and temperature-dependent XRD and emission spectra (PDF)

#### AUTHOR INFORMATION

#### **Corresponding Authors**

Jiyou Zhong - School of Physics and Optoelectronic Engineering, Guangdong University of Technology, Guangzhou 510006, China; orcid.org/0000-0003-2817-6617; Email: zhongjiyou@126.com

Jakoah Brgoch - Department of Chemistry, University of Houston, Houston, Texas 77204, United States; orcid.org/0000-0002-1406-1352; Email: jbrgoch@ uh.edu

#### **Authors**

Liwei Zeng - School of Physics and Optoelectronic Engineering, Guangdong University of Technology, Guangzhou 510006, China

Weiren Zhao - School of Physics and Optoelectronic Engineering, Guangdong University of Technology, Guangzhou 510006, China

Complete contact information is available at: https://pubs.acs.org/10.1021/acsami.2c17902

The authors declare no competing financial interest.

#### **ACKNOWLEDGMENTS**

The authors thank the Guangzhou Basic and Applied Basic Research Project (202201010689), the National Natural Science Foundation of China (51702057), and the National Science Foundation (DMR-1847701).

## REFERENCES

- (1) Grassi, B.; Quaresima, V. Near-Infrared Spectroscopy and Skeletal Muscle Oxidative Function in Vivo in Health and Disease: A Review from an Exercise Physiology Perspective. J. Biomed. Opt. 2016, 21, No. 091313.
- (2) Lucero, A. A.; Addae, G.; Lawrence, W.; Neway, B.; Credeur, D. P.; Faulkner, J.; Rowlands, D.; Stoner, L. Reliability of Muscle Blood Flow and Oxygen Consumption Response from Exercise Using Near-Infrared Spectroscopy. Exp. Physiol. 2018, 103, 90-100.
- (3) Scholkmann, F.; Kleiser, S.; Metz, A. J.; Zimmermann, R.; Mata Pavia, J.; Wolf, U.; Wolf, M. A Review on Continuous Wave Functional Near-Infrared Spectroscopy and Imaging Instrumentation and Methodology. Neuroimage 2014, 85, 6-27.

- (4) Manley, M. Near-Infrared Spectroscopy and Hyperspectral Imaging: Non-Destructive Analysis of Biological Materials. *Chem. Soc. Rev.* **2014**, *43*, 8200–8214.
- (5) Magwaza, L. S.; Opara, U. L.; Nieuwoudt, H.; Cronje, P. J. R.; Saeys, W.; Nicolaï, B. NIR Spectroscopy Applications for Internal and External Quality Analysis of Citrus Fruit—A Review. *Food Bioprocess Technol.* **2012**, *5*, 425–444.
- (6) Marques, E. J. N.; de Freitas, S. T.; Pimentel, M. F.; Pasquini, C. Rapid and Non-Destructive Determination of Quality Parameters in the 'Tommy Atkins' Mango Using a Novel Handheld near Infrared Spectrometer. *Food Chem.* **2016**, *197*, 1207–1214.
- (7) Liu, T.; Cai, H.; Mao, N.; Song, Z.; Liu, Q. Efficient Near-infrared Pyroxene Phosphor LiInGe2O6:Cr3+ for NIR Spectroscopy Application. *J. Am. Ceram. Soc.* **2021**, *104*, 4577–4584.
- (8) Zhong, J.; Zhuo, Y.; Du, F.; Zhang, H.; Zhao, W.; You, S.; Brgoch, J. Efficient Broadband Near-Infrared Emission in the GaTaO4:Cr3+ Phosphor. *Adv. Opt. Mater.* **2022**, *10*, No. 2101800.
- (9) Qiao, J.; Zhang, S.; Zhou, X.; Chen, W.; Gautier, R.; Xia, Z. Near-Infrared Light-Emitting Diodes Utilizing a Europium-Activated Calcium Oxide Phosphor with External Quantum Efficiency of up to 54.7%. *Adv. Mater.* **2022**, 34, No. 2201887.
- (10) Liu, G.; Xia, Z. Modulation of Thermally Stable Photoluminescence in Cr 3+ -Based Near-Infrared Phosphors. *J. Phys. Chem. Lett.* **2022**, 5001–5008.
- (11) Fang, M.-H.; Huang, P.-Y.; Bao, Z.; Majewska, N.; Leśniewski, T.; Mahlik, S.; Grinberg, M.; Leniec, G.; Kaczmarek, S. M.; Yang, C.-W.; Lu, K.-M.; Sheu, H.-S.; Liu, R.-S. Penetrating Biological Tissue Using Light-Emitting Diodes with a Highly Efficient Near-Infrared ScBO3:Cr3+ Phosphor. *Chem. Mater.* **2020**, *32*, 2166–2171.
- (12) Rajendran, V.; Lesniewski, T.; Mahlik, S.; Grinberg, M.; Leniec, G.; Kaczmarek, S. M.; Pang, W.-K.; Lin, Y.-S.; Lu, K.-M.; Lin, C.-M.; Chang, H.; Hu, S.-F.; Liu, R.-S. Ultra-Broadband Phosphors Converted Near-Infrared Light Emitting Diode with Efficient Radiant Power for Spectroscopy Applications. *ACS Photonics* **2019**, *6*, 3215–3224.
- (13) Huang, W.-T.; Cheng, C.-L.; Bao, Z.; Yang, C.-W.; Lu, K.-M.; Kang, C.-Y.; Lin, C.-M.; Liu, R.-S. Broadband Cr3+, Sn4+—doped Oxide Nanophosphors for Infrared Mini Light-Emitting Diodes. *Angew. Chem., Int. Ed.* **2018**, *131*, 2091—2094.
- (14) Li, R.; Liu, Y.; Yuan, C.; Leniec, G.; Miao, L.; Sun, P.; Liu, Z.; Luo, Z.; Dong, R.; Jiang, J. Thermally Stable CaLu2Mg2Si3O12:Cr3+Phosphors for NIR LEDs. *Adv. Opt. Mater.* **2021**, *9*, No. 2100388.
- (15) Zhang, H.; Zhong, J.; Du, F.; Chen, L.; Zhang, X.; Mu, Z.; Zhao, W. Efficient and Thermally Stable Broad-Band Near-Infrared Emission in a KAlP2O7:Cr3+ Phosphor for Nondestructive Examination. ACS Appl. Mater. Interfaces 2022, 14, 11663–11671.
- (16) Zhang, Y.; Miao, S.; Liang, Y.; Liang, C.; Chen, D.; Shan, X.; Sun, K.; Wang, X.-J. Blue LED-Pumped Intense Short-Wave Infrared Luminescence Based on Cr3+-Yb3+-Co-Doped Phosphors. *Light Sci. Appl.* **2022**, *11*, 136.
- (17) Zhang, Q.; Liu, D.; Dang, P.; Lian, H.; Li, G.; Lin, J. Two Selective Sites Control of Cr3+-Doped ABO4 Phosphors for Tuning Ultra-Broadband Near-Infrared Photoluminescence and Multi-Applications. *Laser Photon. Rev.* **2022**, *16*, No. 2100459.
- (18) Liu, D.; Li, G.; Dang, P.; Zhang, Q.; Wei, Y.; Lian, H.; Shang, M.; Lin, C. C.; Lin, J. Simultaneous Broadening and Enhancement of Cr3+ Photoluminescence in LiIn2SbO6 by Chemical Unit Cosubstitution: Night-Vision and Near-Infrared Spectroscopy Detection Applications. *Angew. Chem., Int. Ed.* **2021**, *60*, 14644–14649.
- (19) Basore, E. T.; Xiao, W.; Liu, X.; Wu, J.; Qiu, J. Broadband Near-Infrared Garnet Phosphors with Near-Unity Internal Quantum Efficiency. *Adv. Opt. Mater.* **2020**, *8*, No. 2000296.
- (20) Jia, Z.; Yuan, C.; Liu, Y.; Wang, X.-J.; Sun, P.; Wang, L.; Jiang, H.; Jiang, J. Strategies to Approach High Performance in Cr3+-Doped Phosphors for High-Power NIR-LED Light Sources. *Light Sci. Appl.* **2020**, *9*, 86.
- (21) Huang, X. Red Phosphor Converts White LEDs. *Nat. Photonics* **2014**, *8*, 748–749.

- (22) Qiao, J.; Zhou, G.; Zhou, Y.; Zhang, Q.; Xia, Z. Divalent Europium-Doped near-Infrared-Emitting Phosphor for Light-Emitting Diodes. *Nat. Commun.* **2019**, *10*, 5267.
- (23) Tang, Z.; Zhang, Q.; Cao, Y.; Li, Y.; Wang, Y. Eu2+-Doped Ultra-Broadband VIS-NIR Emitting Phosphor. *Chem. Eng. J.* **2020**, 388, No. 124231.
- (24) Hoerder, G. J.; Seibald, M.; Baumann, D.; Schröder, T.; Peschke, S.; Schmid, P. C.; Tyborski, T.; Pust, P.; Stoll, I.; Bergler, M.; Patzig, C.; Reißaus, S.; Krause, M.; Berthold, L.; Höche, T.; Johrendt, D.; Huppertz, H. Sr[Li2Al2O2N2]:Eu2+—A High Performance Red Phosphor to Brighten the Future. *Nat. Commun.* **2019**, *10*, 1824.
- (25) De Guzman, G. N. A.; Fang, M.-H.; Liang, C.-H.; Bao, Z.; Hu, S.-F.; Liu, R.-S. Near-Infrared Phosphors and Their Full Potential: A Review on Practical Applications and Future Perspectives. *J. Lumin.* **2020**, *219*, No. 116944.
- (26) Zhao, F.; Cai, H.; Song, Z.; Liu, Q. Structural Confinement for Cr3+ Activators toward Efficient Near-Infrared Phosphors with Suppressed Concentration Quenching. *Chem. Mater.* **2021**, *33*, 3621–3630.
- (27) Zhao, M.; Liu, S.; Cai, H.; Zhao, F.; Song, Z.; Liu, Q. Efficient Broadband Near-Infrared Phosphor Sr2ScSbO6:Cr3+ for Solar-like Lighting. *Sci. China Mater.* **2022**, *65*, 1–756.
- (28) Liu, G.; Molokeev, M. S.; Xia, Z. Structural Rigidity Control toward Cr3+-Based Broadband Near-Infrared Luminescence with Enhanced Thermal Stability. *Chem. Mater.* **2022**, *34*, 1376–1384.
- (29) Wang, Y.; Wang, Z.; Wei, G.; Yang, Y.; He, S.; Li, J.; Shi, Y.; Li, R.; Zhang, J.; Li, P. Ultra-Broadband and High Efficiency Near-Infrared Gd3ZnxGa5-2xGexO12:Cr3+ (x = 0-2.0) Garnet Phosphors via Crystal Field Engineering. *Chem. Eng. J.* **2022**, 437, No. 135346.
- (30) You, L.; Tian, R.; Zhou, T.; Xie, R.-J. Broadband Near-Infrared Phosphor BaMgAl10O17: Cr3+ Realized by Crystallographic Site Engineering. *Chem. Eng. J.* **2021**, 417, No. 129224.
- (31) Gao, T.; Zhuang, W.; Liu, R.; Liu, Y.; Yan, C.; Chen, X. Design of a Broadband NIR Phosphor for Security-Monitoring LEDs: Tunable Photoluminescence Properties and Enhanced Thermal Stability. *Cryst. Growth Des.* **2020**, *20*, 3851–3860.
- (32) Wu, H.; Jiang, L.; Li, K.; Li, C.; Zhang, H. Design of Broadband Near-Infrared Y0.57La0.72Sc2.71(BO3)4:Cr3+ Phosphors Based on One-Site Occupation and Their Application in NIR Light-Emitting Diodes. J. Mater. Chem. C 2021, 9, 11761–11771.
- (33) Zhang, Q.; Li, G.; Dang, P.; Liu, D.; Huang, D.; Lian, H.; Lin, J. Enhancing and Tuning Broadband Near-Infrared (NIR) Photoluminescence Properties in Cr3+ -Doped Ca2YHf2Al3O12 Garnet Phosphors via Ce3+ /Yb3+ -Codoping for LED Applications. *J. Mater. Chem. C* 2021, *9*, 4815–4824.
- (34) Liu, G.; Molokeev, M. S.; Lei, B.; Xia, Z. Two-Site Cr3+Occupation in the MgTa2O6:Cr3+ Phosphor toward Broad-Band near-Infrared Emission for Vessel Visualization. *J. Mater. Chem. C* **2020**, *8*, 9322–9328.
- (35) Rajendran, V.; Fang, M.-H.; Guzman, G. N. D.; Lesniewski, T.; Mahlik, S.; Grinberg, M.; Leniec, G.; Kaczmarek, S. M.; Lin, Y.-S.; Lu, K.-M.; Lin, C.-M.; Chang, H.; Hu, S.-F.; Liu, R.-S. Super Broadband Near-Infrared Phosphors with High Radiant Flux as Future Light Sources for Spectroscopy Applications. *ACS Energy Lett.* **2018**, *3*, 2679–2684.
- (36) Zeng, H.; Zhou, T.; Wang, L.; Xie, R.-J. Two-Site Occupation for Exploring Ultra-Broadband Near-Infrared Phosphor—Double-Perovskite La2MgZrO6: Cr3+. *Chem. Mater.* **2019**, 31, 5245–5253.
- (37) He, S.; Zhang, L.; Wu, H.; Wu, H.; Pan, G.; Hao, Z.; Zhang, X.; Zhang, L.; Zhang, H.; Zhang, J. Efficient Super Broadband NIR Ca2LuZr2Al3O12:Cr3+,Yb3+ Garnet Phosphor for Pc-LED Light Source toward NIR Spectroscopy Applications. *Adv. Opt. Mater.* **2020**, *8*, No. 1901684.
- (38) Suo, H.; Wang, Y.; Zhao, X.; Zhang, X.; Li, L.; Guan, K.; Ding, W.; Li, P.; Wang, Z.; Wang, F. Rapid Nondestructive Detection Enabled by an Ultra-Broadband NIR Pc-LED. *Laser Photon. Rev.* **2022**, *16*, No. 2200012.
- (39) Liu, G.; Hu, T.; Molokeev, M. S.; Xia, Z. Li/Na Substitution and Yb3+ Co-Doping Enabling Tunable near-Infrared Emission in

- LiIn2SbO6:Cr3+ Phosphors for Light-Emitting Diodes. *iScience* **2021**, 24, No. 102250.
- (40) Yao, L.; Shao, Q.; Han, S.; Liang, C.; He, J.; Jiang, J. Enhancing Near-Infrared Photoluminescence Intensity and Spectral Properties in Yb3+ Codoped LiScP2O7:Cr3+. *Chem. Mater.* **2020**, *32*, 2430–2439.
- (41) Cai, H.; Liu, S.; Song, Z.; Liu, Q. Tuning Luminescence from NIR-I to NIR-II in Cr 3+ -Doped Olivine Phosphors for Nondestructive Analysis. *J. Mater. Chem. C* **2021**, *9*, 5469–5477.
- (42) He, W.; Wang, Z.; Zheng, T.; Wang, L.; Zheng, S. Origin of the Band Gap Reduction of In-Doped  $\beta$ -Ga2O3. *J. Electron. Mater.* **2021**, 50, 3856–3861.
- (43) Makeswaran, N.; Battu, A. K.; Swadipta, R.; Manciu, F. S.; Ramana, C. V. Spectroscopic Characterization of the Electronic Structure, Chemical Bonding, and Band Gap in Thermally Annealed Polycrystalline Ga2O3 Thin Films. ECS J. Solid State Sci. Technol. 2019, 8, Q3249–Q3253.
- (44) Zhang, J.; Mu, W.; Zhang, K.; Sun, J.; Zhang, J.; Lin, N.; Zhao, X.; Jia, Z.; Tao, X. Broadband Near-Infrared Cr 3+ :β-Ga 2 O 3 Fluorescent Single Crystal Grown by the EFG Method. *CrystEng-Comm* **2020**, 22, 7654–7659.
- (45) Fang, M.-H.; De Guzman, G. N. A.; Bao, Z.; Majewska, N.; Mahlik, S.; Grinberg, M.; Leniec, G.; Kaczmarek, S. M.; Yang, C.-W.; Lu, K.-M.; Sheu, H.-S.; Hu, S.-F.; Liu, R.-S. Ultra-High-Efficiency near-Infrared Ga2O3:Cr 3+ Phosphor and Controlling of Phytochrome. *J. Mater. Chem. C* 2020, *8*, 11013—11017.
- (46) Zhong, J.; Zhuo, Y.; Du, F.; Zhang, H.; Zhao, W.; Brgoch, J. Efficient and Tunable Luminescence in Ga2—XInxO3:Cr3+ for Near-Infrared Imaging. ACS Appl. Mater. Interfaces 2021, 13, 31835—31842.
- (47) Fang, M.-H.; Chen, K.-C.; Majewska, N.; Leśniewski, T.; Mahlik, S.; Leniec, G.; Kaczmarek, S. M.; Yang, C.-W.; Lu, K.-M.; Sheu, H.-S.; Liu, R.-S. Hidden Structural Evolution and Bond Valence Control in Near-Infrared Phosphors for Light-Emitting Diodes. *ACS Energy Lett.* **2021**, *6*, 109–114.
- (48) Shannon, R. D. Revised Effective Ionic Radii and Systematic Studies of Interatomic Distances in Halides and Chalcogenides. *Acta Crystallogr. Sect. A* **1976**, 32, 751–767.
- (49) Xu, X.; Shao, Q.; Yao, L.; Dong, Y.; Jiang, J. Highly Efficient and Thermally Stable Cr3+-Activated Silicate Phosphors for Broadband near-Infrared LED Applications. *Chem. Eng. J.* **2020**, 383, No. 123108.
- (50) Toby, B. H. EXPGUI, a Graphical User Interface for GSAS. J. Appl. Crystallogr. 2001, 34, 210–213.
- (51) Hafner, J. Ab-Initio Simulations of Materials Using VASP: Density-Functional Theory and Beyond. *J. Comput. Chem.* **2008**, 29, 2044–2078.
- (52) Perdew, J. P.; Burke, K.; Ernzerhof, M. Generalized Gradient Approximation Made Simple. *Phys. Rev. Lett.* **1996**, *77*, 3865–3868.
- (53) Kresse, G.; Hafner, J. Ab Initio Molecular Dynamics for Liquid Metals. *Phys. Rev. B* **1993**, *47*, 558–561.
- (54) Kresse, G.; Furthmüller, J. Efficient Iterative Schemes for Ab Initio Total-Energy Calculations Using a Plane-Wave Basis Set. *Phys. Rev. B* **1996**, *54*, 11169–11186.
- (55) Hohenberg, P.; Kohn, W. Inhomogeneous Electron Gas. *Phys. Rev.* **1964**, *136*, B864–B871.
- (56) Makuła, P.; Pacia, M.; Macyk, W. How To Correctly Determine the Band Gap Energy of Modified Semiconductor Photocatalysts Based on UV-Vis Spectra. *J. Phys. Chem. Lett.* **2018**, *9*, 6814–6817.
- (57) Bai, B.; Dang, P.; Huang, D.; Lian, H.; Lin, J. Broadband Near-Infrared Emitting Ca2LuScGa2Ge2O12:Cr3+ Phosphors: Luminescence Properties and Application in Light-Emitting Diodes. *Inorg. Chem.* **2020**, *59*, 13481–13488.
- (58) Baur, W. H. The Geometry of Polyhedral Distortions. Predictive Relationships for the Phosphate Group. *Acta Crystallogr., Sect. B: Struct. Crystallogr. Cryst. Chem.* **1974**, *30*, 1195–1215.
- (59) Struve, B.; Huber, G. The Effect of the Crystal Field Strength on the Optical Spectra of Cr3+ in Gallium Garnet Laser Crystals. *Appl. Phys. B: Lasers Opt.* **1985**, *36*, 195–201.
- (60) Rajendran, V.; Fang, M.-H.; Huang, W.-T.; Majewska, N.; Lesniewski, T.; Mahlik, S.; Leniec, G.; Kaczmarek, S. M.; Pang, W. K.;

- Peterson, V. K.; Lu, K.-M.; Chang, H.; Liu, R.-S. Chromium Ion Pair Luminescence: A Strategy in Broadband Near-Infrared Light-Emitting Diode Design. *J. Am. Chem. Soc.* **2021**, *143*, 19058–19066.
- (61) Wang, Y.; Wang, Z.; Wei, G.; Yang, Y.; He, S.; Li, J.; Shi, Y.; Li, R.; Zhang, J.; Li, P. Highly Efficient and Stable Near-Infrared Broadband Garnet Phosphor for Multifunctional Phosphor-Converted Light-Emitting Diodes. *Adv. Opt. Mater.* **2022**, *10*, No. 2200415.
- (62) Fan, J.; Ai, Y.; Zhou, W.; Luo, J.; Lin, L.; Zhou, J.; Pang, Q.; Zhou, L.; Zhang, T.; Zhang, X. NIR Emission Spectral Engineering in NaSc(Si,Ge)2O6: Cr3+ Solid-Solution Phosphors via Crystal Field Regulation. J. Lumin. 2022, 2022, No. 118887.
- (63) Tan, T.; Wang, S.; Su, J.; Yuan, W.; Wu, H.; Pang, R.; Wang, J.; Li, C.; Zhang, H. Design of a Novel Near-Infrared Luminescence Material Li2Mg3TiO6:Cr3+with an Ultrawide Tuning Range Applied to Near-Infrared Light-Emitting Diodes. *ACS Sustainable Chem. Eng.* **2022**, *10*, 3839–3850.
- (64) Yao, L.; Shao, Q.; Shi, M.; Shang, T.; Dong, Y.; Liang, C.; He, J.; Jiang, J. Efficient Ultra-Broadband Ga4GeO8:Cr 3+ Phosphors with Tunable Peak Wavelengths from 835 to 980 Nm for NIR Pc-LED Application. *Adv. Opt. Mater.* **2022**, *10*, No. 2102229.
- (65) Kim, Y. H.; Arunkumar, P.; Kim, B. Y.; Unithrattil, S.; Kim, E.; Moon, S.-H.; Hyun, J. Y.; Kim, K. H.; Lee, D.; Lee, J.-S.; Im, W. B. A Zero-Thermal-Quenching Phosphor. *Nat. Mater.* **2017**, *16*, 543–550.
- (66) Song, E.; Ming, H.; Zhou, Y.; He, F.; Wu, J.; Xia, Z.; Zhang, Q. Cr3+-Doped Sc-Based Fluoride Enabling Highly Efficient Near Infrared Luminescence: A Case Study of K2NaScF6:Cr3+. *Laser Photon. Rev.* **2021**, *15*, No. 2000410.
- (67) Lin, Q.; Wang, Q.; Liao, M.; Xiong, M.; Feng, X.; Zhang, X.; Dong, H.; Zhu, D.; Wu, F.; Mu, Z. Trivalent Chromium Ions Doped Fluorides with Both Broad Emission Bandwidth and Excellent Luminescence Thermal Stability. ACS Appl. Mater. Interfaces 2021, 13, 18274–18282.
- (68) He, F.; Song, E.; Zhou, Y.; Ming, H.; Chen, Z.; Wu, J.; Shao, P.; Yang, X.; Xia, Z.; Zhang, Q. A General Ammonium Salt Assisted Synthesis Strategy for Cr3+ -Doped Hexafluorides with Highly Efficient Near Infrared Emissions. *Adv. Funct. Mater.* **2021**, 31, No. 2103743.
- (69) Amachraa, M.; Wang, Z.; Chen, C.; Hariyani, S.; Tang, H.; Brgoch, J.; Ong, S. P. Predicting Thermal Quenching in Inorganic Phosphors. *Chem. Mater.* **2020**, *32*, 6256–6265.
- (70) Brgoch, J.; DenBaars, S. P.; Seshadri, R. Proxies from Ab Initio Calculations for Screening Efficient Ce3+ Phosphor Hosts. *J. Phys. Chem. C* 2013, 117, 17955–17959.